

Magnetic field evolution of the K2 dwarf V471 Tau

B. Zaire^{1*}, J.-F. Donati¹, and B. Klein²

¹*IRAP, Université de Toulouse, CNRS / UMR 5277, CNES, UPS, 14 avenue E. Belin, Toulouse, F-31400 France*

²*Sub-department of Astrophysics, Department of Physics, University of Oxford, Oxford, OX1 3RH, UK*

Accepted XXX. Received YYY; in original form ZZZ

ABSTRACT

Observations of the eclipsing binary system V471 Tau show that the time of the primary eclipses varies in an apparent periodic way. With growing evidence that the magnetically active K2 dwarf component might be responsible for driving the eclipse timing variations (ETVs), it is necessary to monitor the star throughout the predicted ~ 35 yr activity cycle that putatively fuels the observed ETVs. We contribute to this goal with this paper by analysing spectropolarimetric data obtained with ESPaDOnS at the Canada-France-Hawaii Telescope in December 2014 and January 2015. Using Zeeman-Doppler Imaging, we reconstruct the distribution of brightness inhomogeneities and large-scale magnetic field at the surface of the K2 dwarf. Compared to previous tomographic reconstructions of the star carried out with the same code, we probe a new phase of the ETVs cycle, offering new constraints for future works exploring whether a magnetic mechanism operating in the K2 dwarf star is indeed able to induce the observed ETVs of V471 Tau.

Key words: Magnetic fields – stars: magnetic field – stars: imaging – stars: individual: V471 Tau – binaries: eclipsing – techniques: polarimetric

1 INTRODUCTION

Several eclipsing binary systems display periodic eclipse timing variations (ETVs) when considering a linear ephemeris to predict the time of mid-eclipse (Lanza et al. 1998; Lanza & Rodonò 1999; Zorotovic & Schreiber 2013; Bours et al. 2016). It is estimated that around 90 per cent of the post-common-envelope binary (PCEB) systems display ETVs (Zorotovic & Schreiber 2013). The main explanations that have been proposed to account for the existence of ETVs are associated with the presence of circumbinary bodies perturbing the orbit of the system (Irwin 1952) or magnetically-induced gravitational modulations caused by an active star in the system (Applegate & Patterson 1987; Applegate 1992; Lanza et al. 1998; Lanza 2005, 2006, 2020; Völschow et al. 2016, 2018). In most cases, ETVs are attributed to circumbinary planet/sub-stellar components that, given their mass and orbital distance, can explain the periodicity and amplitude of ETVs (Parsons et al. 2010; Rappaport et al. 2013; Conroy et al. 2014; Marsh et al. 2014; Hajdu et al. 2019; Marcadon et al. 2020; Papageorgiou et al. 2021). However, recent investigations showed that caution must be taken when interpreting ETVs as caused by circumbinary objects (e.g., Marsh 2018). In particular, some of the circumbinary objects inferred from the ETVs have been refuted afterwards using dynamical stability analysis (Horner et al. 2011, 2012, 2014; Wittenmyer et al. 2012; Marsh 2018; Mai & Mutel 2021) or high-resolution direct imaging of the systems (e.g. V471 Tau, Hardy et al. 2015).

V471 Tau is a close binary system consisting of a K2 dwarf main-sequence star and a hot white dwarf (Nelson & Young 1970). The system has a short orbital period of $P_{\text{orb}} = 0.5211833875$ day (Vac-

caro et al. 2015) and due to tides the K2 dwarf is forced to rotate nearly synchronously with the orbital period ($P_{\text{rot}} \approx P_{\text{orb}}$). As in most PCEBs, cyclic ETVs are observed in V471 Tau with typical modulations of semi-amplitude $\Delta P/P_{\text{orb}} \approx 8.5 \times 10^{-7}$ (where ΔP is the difference between the observed orbital period minus the mean orbital period P_{orb}) and periodicity of 30–35 yr (Kundra & Hric 2011; Vaccaro et al. 2015; Marchioni et al. 2018; Lanza 2020). Guinan & Ribas (2001) analysed whether the gravity influence of a hypothetical third body could lead to the ETVs of the system. The authors found that V471 Tau would need a brown dwarf component with a mass of $\approx 0.0393 \pm 0.0038 M_{\odot}$ and a semi-major axis of 11.2 ± 0.4 AU to reconcile the amplitude and periodicity of the ETV cycle. However, an image of V471 Tau obtained with SPHERE at the Very Large Telescope (VLT) refuted the existence of the brown dwarf (Hardy et al. 2015). This view is supported by Vanderbosch et al. (2017), who dismissed the brown dwarf component using different arguments based on the lack of temporal variations of the rotational period of the white dwarf (that otherwise should vary with the same periodicity of the ETVs due to the barycenter wobbling).

Alternative effects of magnetic origin have thus been put forward as the most probable cause of ETVs in V471 Tau (e.g., Applegate 1992; Völschow et al. 2016; Navarrete et al. 2018, 2020; Lanza 2020). Despite differences between the proposed models, a common feature that they all share relies on the magnetism of the active component in V471 Tau – i.e., the K2 dwarf star. The Applegate effect (Applegate 1992) explains ETVs as an indirect outcome of the redistribution of angular momentum within the convective zone of the K2 dwarf throughout a magnetic cycle. The main idea behind the model is that the redistribution of angular momentum causes temporal modulation of the gravitational quadrupole moment of the K2 dwarf. This increases (resp. decreases) the gravitational field at the orbital

* E-mail: bonnie.zaire@irap.omp.eu

plane forcing the white dwarf component to orbit closer to (resp. further from) the K2 dwarf and with shorter (resp. longer) periods to conserve the total angular momentum of the system (thus creating ETVs). Besides, activity studies suggest a cyclic nature for the magnetism of the K2 dwarf yielding a putative period of about 13 yr (İbanoğlu et al. 2005; Kamiński et al. 2007; Pandey & Singh 2008; Kóvári et al. 2021). However, the feasibility of the Applegate mechanism in V471 Tau has been debated ever since Applegate (1992) as it requires significant variations of the differential rotation that are yet to be detected at the surface of the K2 dwarf (see discussions of Lanza 2005, 2006; Völschow et al. 2016, 2018; Zaire et al. 2021).

Lanza (2020) proposed a new mechanism (hereinafter the Lanza mechanism) that requires lower variations of the differential rotation at the surface of the K2 dwarf to explain the ETVs. This new model is based on the existence of a non-axisymmetric gravitational quadrupole moment induced by a non-axisymmetric stationary field throughout the convective zone of the K2 dwarf. Similar to the Applegate effect, the idea behind the Lanza effect is that the modulation of the gravitational field along the line joining both stars generates ETVs. However, the Lanza effect provides a novel approach to the source of variation of the gravitational field, which results from a non-axisymmetric stationary magnetic field that is forced to librate around the Lagrange L1 point of the system or to circulate monotonically in the orbital plane. The Lanza mechanism has been shown to reduce by at least an order of magnitude the required fluctuation amplitude of the differential rotation with respect to the Applegate effect. Nevertheless, in order for the Lanza effect to explain the ETVs of V471 Tau the non-axisymmetric field needs to librate/circulate with a period of 70 yr, which disagrees with the 13 yr activity cycle proposed from recent observations of the K2 dwarf (Kóvári et al. 2021). Therefore, the origin of ETVs on V471 Tau is still unclear and demonstrating whether an Applegate effect, a Lanza effect, or another effect of magnetic origin operates in the system requires dedicated studies of the K2 dwarf magnetism.

Recently, Zaire et al. (2021, hereafter Paper I) reported first large scale surface magnetic maps and offered new differential rotation measurements of the K2 dwarf for two different epochs (November/December 2004 and December 2005). They found that the K2 dwarf exhibits significant fluctuations in its differential rotation amplitude (ranging from the solar value to about twice the solar differential rotation in a year) and it is not always rotating as a solid body as it was reported to in an early study (Hussain et al. 2006). Despite providing useful information to disentangle the magnetic effects proposed to explain ETVs in V471 Tau, this initial study only probed a maximum of the ETVs cycle at which differential rotation is not expected to peak in the Applegate scenario. Additional surface maps and shear measurements probing different phases of the ETV cycle are thus still needed to determine the fluctuation amplitude of the surface shear and to search for a possible long term evolution, perhaps following the prediction of Applegate or Lanza, of the surface magnetic field of the K2 dwarf.

In this study, we reconstruct new large-scale magnetic field maps and perform new differential rotation measurements of the K2 dwarf of V471 Tau in December 2014/January 2015, probing a new phase of the ETV modulation cycle in which the observed orbital period is close to the mean orbital period $P_{\text{orb}} = 0.5211833875$ day (Vaccaro et al. 2015). Section 2 describes the spectropolarimetric observations and, Section 3, presents the tomographic reconstructions and the differential rotation measurements. Finally, we discuss our results and conclude in Section 4.

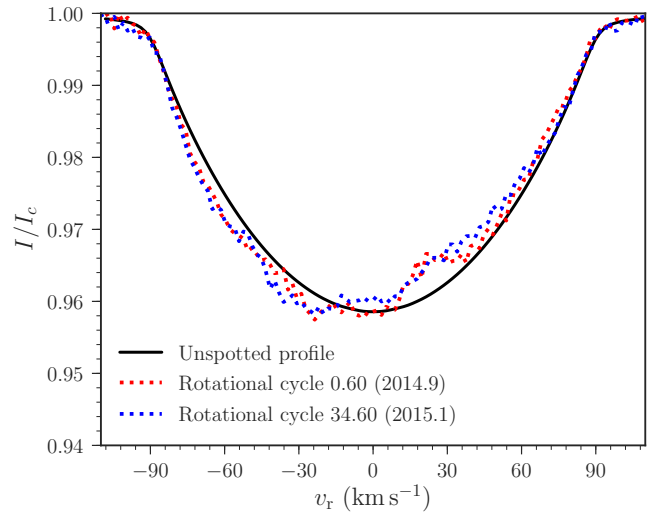


Figure 1. Observed Stokes I LSD profiles at the rotational phase 0.6 (dotted lines) and absorption line profile computed for an unspotted star with $v \sin i = 89.3 \pm 0.1 \text{ km s}^{-1}$ (black continuous line). The two profiles correspond to observations at the same rotational phase in 2014.9 (red) and 2015.1 (blue). Rotational cycles (starting from cycle 21470) are indicated.

2 OBSERVATIONS

We use spectropolarimetric observations of V471 Tau collected with ESPaDOnS at the Canada-France-Hawaii Telescope. The optical spectropolarimeter ESPaDOnS covers wavelengths from 370 to 1,000 nm at a resolving power of 65,000 (Donati 2003; Donati et al. 2006a). Our data set consists of 236 unpolarised (Stokes I), and 59 circularly polarised (Stokes V) profiles acquired in 11 nights spread between 20 December 2014 and 12 January 2015. Circularly-polarised spectra are computed combining 4 sub-exposures of 200 s each taken at different orientations of the polarimeter retarders combined in an optimal way to minimize potential spurious signatures and to remove systematics in the circularly polarised spectra (Donati et al. 1997). The data reduction was carried out with the pipeline Libre-ESPRIT optimized for ESPaDOnS observations (Donati et al. 1997). The observational logbook is given in Table A1. Circularly polarised spectra show peak signal-to-noise ratios (SNRs) ranging from 122 to 212 (per 1.8 km s^{-1} spectral pixel), with a median of 184. Orbital cycles E are computed according to the ephemeris of Vaccaro et al. (2015):

$$\text{HJED} = 2445821.898291 + 0.5211833875 \times E, \quad (1)$$

where phase 0.5 corresponds to the K2 dwarf mid-eclipse (i.e., when the white dwarf is in front of the K2 star). Moreover, because the K2 dwarf rotates nearly synchronously, its rotational cycle is equal to the orbital cycle E .

In order to generate averaged photospheric lines of the K2 dwarf with enhanced SNRs, we applied Least-Squares Deconvolution (LSD Donati et al. 1997) on all absorption lines with a relative depth of at least 40% with respect to the continuum. Figure 1 shows two example Stokes I LSD profiles obtained at rotational phase 0.6 using the same K2 dwarf absorption line mask detailed in Paper I. Observed Stokes I LSD profiles show clear distortions with respect to the absorption line shape of an unspotted stellar surface assuming a line-of-sight projected equatorial velocity of $v \sin i = 89.3 \pm 0.11 \text{ km s}^{-1}$ (Vaccaro et al. 2015, Paper I). These Stokes I signatures provide evidence for brightness inhomogeneities at the surface of the K2 dwarf star (i.e.,

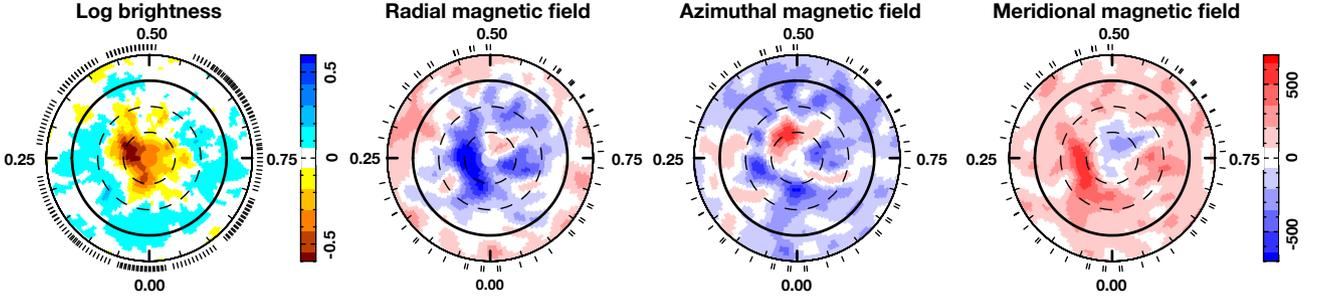


Figure 2. Tomographic reconstruction of the K2 dwarf surface using both 2014.9 and 2015.1 data sets. The star is shown in a flattened polar view with concentric circles representing 30° steps in latitude. Ticks outside the star indicate the rotational phase of our observations. The first plot shows the brightness distribution, where cool spots are shown as brown shades and warm plages as blue shades. The following plots show respectively the radial, azimuthal, and meridional components of the large-scale magnetic field in spherical coordinates. Magnetic fields are expressed in Gauss, with positive values represented in red shades and negative in blue.

signatures within $\pm v \sin i$), similar to what was found in previous Doppler images of this star (Ramseyer et al. 1995; Hussain et al. 2006; Paper I; Kóvári et al. 2021). Moreover, the shape difference of line profiles collected at the same rotational phase but different rotation cycles suggests that the brightness distribution evolves on a timescale of a few weeks.

3 RESULTS

We apply the Zeeman-Doppler imaging technique (ZDI) to the time series of Stokes I or Stokes V LSD profiles to simultaneously reconstruct the surface brightness distribution and the large-scale magnetic field topology. To do so, ZDI models the stellar surface as a grid of a few thousand cells, whose individual contributions to the total synthetic Stokes profiles are computed using the analytical solution of Unno-Rachkovsky to the polarised radiative transfer equations in a Milne-Eddington atmosphere (see Landi Degl’Innocenti & Landolfi 2004). The ZDI code inverts the observed LSD profiles into surface images using a conjugate gradient algorithm that searches for the maximum-entropy image that reproduces the data down to a reduced χ^2 of about unity (Donati et al. 1989; Brown et al. 1991; Donati & Brown 1997; Donati et al. 2006b). The entropy of each image is computed considering individual cells for the brightness maps, while it is a function of spherical harmonics coefficients for the magnetic maps. As in Paper I, the magnetic field expansion is limited to spherical harmonics with order $\ell \leq 15$.

Our tomographic reconstruction follows closely the procedures described in Paper I, where we reconstructed brightness and large-scale magnetic surface maps of the K2 dwarf V471 Tau at two early epochs (2004.9 and 2005.9). In a first step, we use ZDI to optimise the orbital motion correction by reconstructing surface spots from our set of Stokes I profiles. Using a fixed semi-amplitude of $K = 149.3 \text{ km s}^{-1}$ (Paper I), we reconstruct several brightness surface maps by varying the systemic velocity (v_γ) and phase offset (ϕ_0) assuming the ephemeris of Equation 1. We find that, at constant information at the surface of the star, the best parameters reproducing the observations are $v_\gamma = 35.0 \pm 0.10 \text{ km s}^{-1}$ and $\phi_0 = 0.0025 \pm 0.0005$.

In all the image reconstructions that follow, we use the orbital parameters derived above to correct the spectra from Doppler shifts before applying ZDI. Akin to Paper I, we fix the line-of-sight projected equatorial velocity and the stellar inclination angle to $v \sin i = 89.3 \pm 0.11 \text{ km s}^{-1}$ and $i = 78.755 \pm 0.030^\circ$ (Vaccaro et al. 2015), respectively. We also recall that, due to the difficulty of

ZDI to distinguish features from Northern and Southern hemispheres in nearly equator-on stars (Vogt et al. 1987; Rice et al. 1989; Unruh & Collier Cameron 1995; Şenavcı et al. 2018; Lehmann et al. 2019; Hahlin et al. 2021), the reconstructed images may be subject to some mirroring effect with respect to the equator, to the same extent as those presented in Paper I. In practice, this effect is expected to be mitigated by the excellent phase coverage of our data set (e.g. see Vincent et al. 1993).

3.1 Brightness and magnetic imaging

We first attempt at reconstructing the surface maps of the K2 dwarf star using the LSD profiles collected in 2014.9 and 2015.1. Applying ZDI to the Stokes I LSD profiles (Stokes V LSD) shows that the data can only be fitted down to a reduced χ^2 of 1.47 (1.15) when assuming that the star rotates as a solid body. When assuming differential rotation (see Section 3.2), the Stokes I data can now be fitted down to a reduced χ^2 of 1.10 and Stokes V data to 1.07.

Figure 2 shows the maps obtained after including differential rotation in our image reconstruction process. The brightness map recovered for the combined 2014.9 and 2015.1 data set shows inhomogeneities with respect to the unperturbed photosphere (with an effective temperature of about 5066 K). It features a cool polar cap with low-latitude appendages that extend down to 30° latitude. As in Paper I, we find that warm low-contrast plages forming a partial ring structure are also present at low latitudes. From the brightness map we obtain that 10% of the stellar surface is covered with cool spots and 8% with warm plages.

The reconstructed large-scale magnetic field is also shown in Figure 2. We find an average magnetic field strength of 360 G. It shows up from the surface maps that strong negative radial fields (reaching strengths up to 500 G) overlap with the high-contrast cool spots forming the polar cap. The overall magnetic topology that we obtain is dominated by the poloidal component, whereas the toroidal magnetic energy accounts for 25% of the total energy. The poloidal field features a strong dipole mode (containing 60% of the poloidal energy), while other spherical harmonics modes with order $\ell \geq 4$ contribute altogether to 30% of the poloidal energy. We also find that 75% of the poloidal energy is stored in axisymmetric modes with $m < \ell/2$. The dipolar component has a polar strength of 335 G and is tilted by 7° towards phase 0.87.

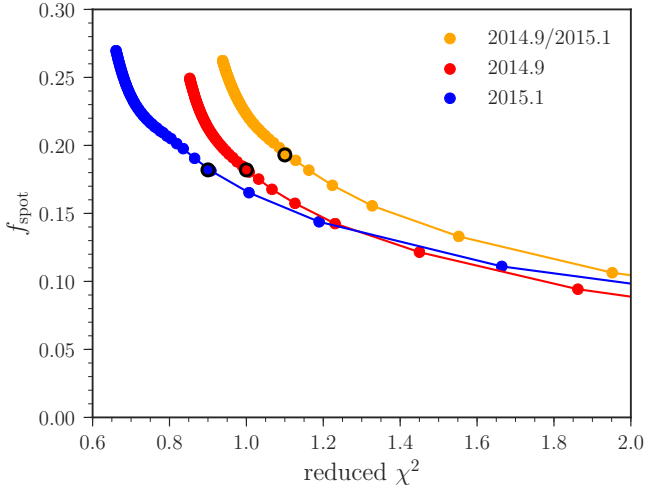


Figure 3. Spot coverage (f_{spot}) as a function of the reduced χ^2 for a tomographic reconstruction process aiming at a low value of reduced χ^2 and including differential rotation (see Section 3.2). Curves with different colors show reconstructions using different Stokes I data sets (see legend). Black circles highlight the values when the spot coverage sharply rises for a decreasing reduced χ^2 .

3.1.1 Short-term variability

We find that even after including differential rotation in our image reconstruction process, the total data set can only be fitted down to a reduced χ^2 of 1.1 when using Stokes I profiles and 1.07 when using Stokes V . This suggests that the surface brightness and magnetic maps evolve on a timescale of a few weeks. To explore whether a short-term evolution indeed occurs, we split the total data set in two. The first subset gathers spectra from 2014.9 (totalling 132 Stokes I profiles and 33 Stokes V spread over 6 non-consecutive nights) and the other combines spectra from 2015.1 (104 Stokes I profiles and 26 Stokes V collected over 5 nights).

Figure 3 shows the spot coverage at different iterations of the ZDI reconstruction process when we aim at fitting the time series of Stokes I profiles at a progressively lower reduced χ^2 . The data illustrates how ZDI adds spots at the stellar surface to better fit the observations. We can see in this figure that the spot coverage sharply increases below a given reduced χ^2 (whose value depends on the data set). This behavior suggests that below this reduced χ^2 threshold, the tomographic imaging process starts to fit noise features present in the data. Using the slope of the curves in Figure 3 as a criteria to define the reduced χ^2 at which the ZDI reconstruction process aims (e.g., see Alvarado-Gómez et al. 2015, for a detailed explanation about using derivatives as a stop-criteria), we find that the Stokes I subsets of 2014.9 and 2015.1 can be fitted down to a reduced χ^2 of 1.0 and 0.9, respectively.

Figure 4 shows the brightness and magnetic maps obtained for the individual subsets including differential rotation. Whereas the maps derived in 2014.9 and 2015.1 look similar at first order, we observe small differences reflecting an intrinsic evolution of the brightness and magnetic field of the K2 dwarf. Starting from the brightness maps, we note a visible decrease in the contrast of the cool spot at the polar cap and tiny azimuthal rearrangements in the distribution of warm plages. As a result, the K2 dwarf surface appears slightly less spotted in 2015.1. We find that warm plages cover 7% of the

Table 1. Magnetic field properties of the K2 dwarf star. B_{rms} is the root-mean-square field, B_{dip} is the dipolar strength, and E_{pol} is the fractional energy in the poloidal field. $E_{\ell=1}$, $E_{\ell=2}$, $E_{\ell=3}$ and $E_{\ell \geq 4}$ are, respectively, the fractional energies of the dipolar, quadrupolar, octupolar, and multipolar (defined as $\ell \geq 4$) components.

	Data set		
	2014.9/2015.1	2014.9	2015.1
B_{rms} (G)	360 ± 7	415 ± 5	335 ± 6
B_{dip} (G)	-335 ± 20	-440 ± 35	-250 ± 26
θ_{dip} ($^\circ$)	7 ± 5	9 ± 2	9 ± 3
E_{pol} (%)	75 ± 5	80 ± 5	70 ± 3
$E_{\ell=1}$ (%)	55 ± 5	60 ± 9	45 ± 7
$E_{\ell=2}$ (%)	5 ± 5	5 ± 2	5 ± 2
$E_{\ell=3}$ (%)	5 ± 2	5 ± 2	5 ± 2
$E_{\ell \geq 4}$ (%)	35 ± 4	30 ± 9	45 ± 7

surface in both maps, while dark spots covered 10% of the stellar surface in 2014.9 and 9% in 2015.1. Regarding magnetic maps, we find that the negative radial field covers a larger portion of the North pole in 2014.9 than 2015.1 (see Figure 4). As expected, the brightness and magnetic maps derived from the original data set (Figure 2) resemble an average of the individual maps derived from the subsets. Table 1 summarises the magnetic properties derived from the split and original data sets. We assess the uncertainties in the image reconstruction process using the bootstrap technique detailed in Paper I.

3.2 Differential rotation

As mentioned in Subsection 3.1, the global data set 2014.9/2015.1 cannot be fitted down to a reduced χ^2 of 1 as a result of temporal evolution of surface maps. One of the potential sources for this evolution is the presence of differential rotation at the surface of the K2 dwarf star.

The ZDI code allows one to explore whether stars rotate differentially by searching for recurrent distortions in the line profiles of our spectropolarimetric time series (Donati et al. 2000). To do so, ZDI incorporates in the image reconstruction process a predefined latitudinal differential rotation law given by

$$\Omega(\theta) = \Omega_{\text{eq}} - d\Omega \sin^2(\theta), \quad (2)$$

where Ω is the latitudinal angular velocity profile, θ is the latitude, Ω_{eq} is the angular velocity at the equator, and $d\Omega$ is the difference between Ω_{eq} and the angular velocity at the pole. Brightness and magnetic maps are thus individually reconstructed for each pair of $(\Omega_{\text{eq}}, d\Omega)$ values, with a χ^2 value attributed to each tomographic reconstruction (carried out at constant information content for all pairs of differential rotation parameters). Figure 5 shows the resulting confidence levels for the differential rotation parameters, when reconstructing the brightness surface distribution (i.e., using Stokes I alone) and the magnetic topology (i.e., using Stokes V alone). Using the minimum of the paraboloid and its local curvature to retrieve the optimal shear parameters and corresponding error bars (Donati et al. 2003), we obtain $d\Omega = 60 \pm 1 \text{ mrad d}^{-1}$ and $\Omega_{\text{eq}} = 12.084 \pm 0.001 \text{ rad d}^{-1}$ from the χ^2 distribution using Stokes I , and $d\Omega = 42 \pm 3 \text{ mrad d}^{-1}$ and $\Omega_{\text{eq}} = 12.077 \pm 0.001 \text{ rad d}^{-1}$ from the χ^2 distribution using Stokes V . As in Paper I, these results again suggest that brightness inhomogeneities and magnetic structures are sheared by different amounts.

Moreover, we use ten bootstrapped data sets to estimate the differential rotation parameters uncertainty associated with the image

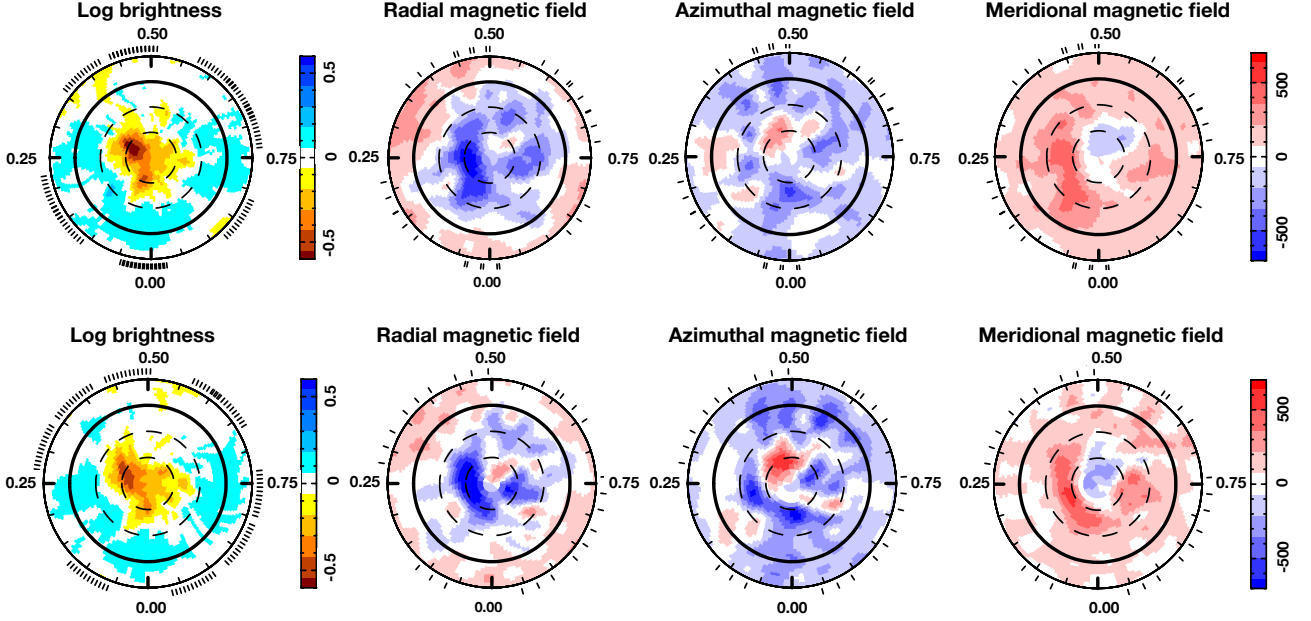


Figure 4. ZDI reconstruction of the individual subsets of 2014.9 (top panels) and 2015.1 (bottom panels). Surface maps are illustrated in a similar fashion to Figure 2.

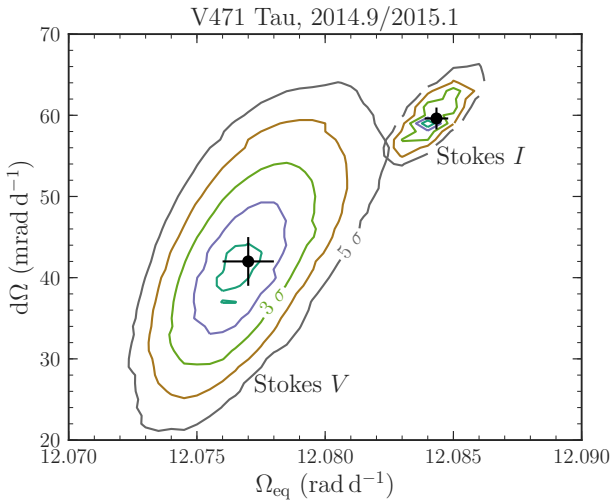


Figure 5. Differential rotation measurements obtained with the sheared-imaging method using Stokes *I* or Stokes *V* profiles. Contour levels represent confidence levels up to 5σ . Black circles represent the best-fit obtained after assuming a paraboloid distribution.

reconstruction process (see details in Paper I). To do that, we repeat the steps above to determine the differential rotation parameters using bootstrapped Stokes *I* or Stokes *V* profiles. From the χ^2 maps obtained using bootstrapped data sets, we find that the mean values of the ten error bars obtained using Stokes *I* and Stokes *V* profiles are similar to the error bars obtained from the original data.

3.3 H α variability

The variability of H α in V471 Tau has been reported by several authors (Young et al. 1991; Rottler et al. 2002; Kóvári et al. 2021, Paper I). The dynamical spectra of the H α line in 2014.9/2015.1 is plotted in Figure 6. Starting with the radial velocity range within $\pm v \sin(i)$, we identify that H α exhibits the typical rotational modulation at the the K2 dwarf surface. H α is in emission on the stellar hemisphere that faces the white dwarf and in absorption on the opposite hemisphere. The H α equivalent width reveals a peak-to-peak amplitude of about 1.2 \AA with a maximum emission of -0.5 \AA at phase 0.5.

Further, we observe a modulated emission with an amplitude of $205 \pm 40 \text{ km s}^{-1}$ in the rest frame of the K2 dwarf (see Figure 6). We speculate that this emission is due to a stable prominence trapped at $2.30 \pm 0.45 R_{\star}$ from the K2 dwarf (or, equivalently, at $1.29 \pm 0.45 R_{\star}$ from the white dwarf component). We find a full width at half maximum (FWHM) of 1.89 \AA and an equivalent width of about -0.17 \AA when fitting a Gaussian to the prominence emission at phase 0.75. Assuming that the prominence is spherical, we estimate a prominence radius of about $0.50 R_{\star}$ from its FWHM emission in H α .

4 DISCUSSIONS AND CONCLUSIONS

In this paper, we analysed new spectropolarimetric data of the binary system V471 Tau collected from 20 December 2014 to 12 January 2015 with ESPaDOnS. Using Zeeman-Doppler imaging, we modelled time series of LSD Stokes *I* and *V* profiles to recover new brightness and magnetic maps of the K2 dwarf component of V471 Tau.

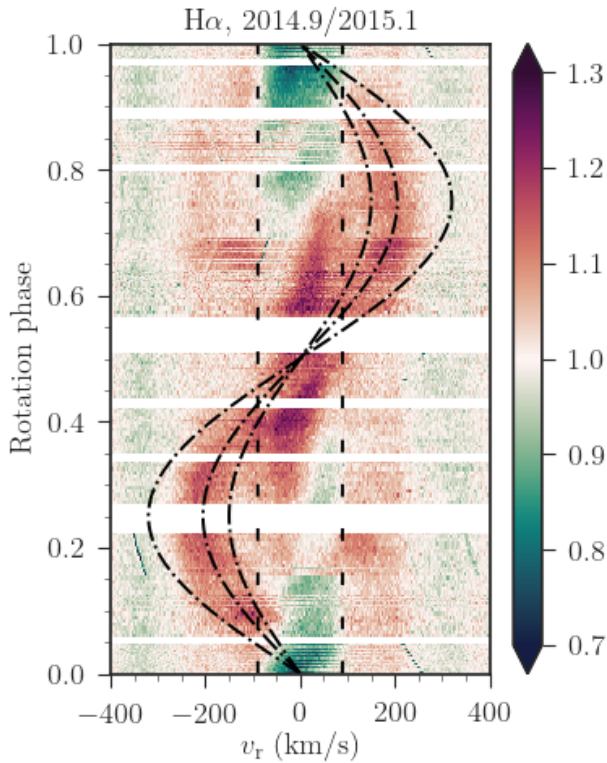


Figure 6. Dynamical spectra of $H\alpha$ shown in the rest frame of the K2 dwarf. Red shades indicate that $H\alpha$ is in emission and green shades in absorption. The vertical dashed lines correspond to the stellar rotational broadening of $\pm v \sin(i)$. Sine waves of semi-amplitudes 150 km s^{-1} (center of mass), 205 km s^{-1} (prominence position), and 320 km s^{-1} (white dwarf position) are over-plotted as dashed-dotted lines.

4.1 Brightness map, magnetic field topology, and differential rotation

Our brightness image reveals a strong cool polar cap in 2014.9/2015.1. This result is confirmed by an independent Doppler imaging reconstruction using a different inversion code (Kóvári et al. 2021). Along with previous brightness maps (Ramseyer et al. 1995; Hussain et al. 2006; Paper I), we find that the cool polar cap seen in the star surface is stable in a timescale of years. The spot coverage of $\approx 18\%$ derived in 2014.9/2015.1 is in good agreement with what is expected from photometry (in the range 15–25%, see Paper I) suggesting that most of the brightness spots generating photometric fluctuations in V471 Tau are large enough to be detected and resolved by Doppler imaging.

The reconstructed large scale magnetic field shows a dominant poloidal component that accounts for about 75% of the magnetic energy in 2014.9/2015.1. This value is slightly larger than those observed in 2004.9 and 2005.9, whose fractional poloidal energy corresponded to 70% and 60%, respectively. Moreover, we find that the dipole strength in 2014.9/2015.1 is about 3.6 times stronger than that in 2004.9 and 2005.9.

We also confirmed that the surface of the K2 dwarf is differentially rotating. We measured an equatorial to pole angular velocity difference of 60 and 42 mrad d^{-1} from spot and magnetic structures, respectively. This finding confirms the solar-like differential rotation profile obtained for the star in 2004.9 and 2005.9 (Paper I).

Interestingly, the shear level inferred from our 2014.9/2015.1 data set resembles closely those obtained nine years before (73 and 48 mrad d^{-1} in 2005.9; Paper I).

4.2 Magnetic activity

Studies of chromospheric/coronal activity indicators (Rottler et al. 2002; Kamiński et al. 2007; Pandey & Singh 2008; Kóvári et al. 2021) and long-term photometry (Skillman & Patterson 1988; İbanoğlu et al. 2005) of the K2 dwarf suggest an activity cycle of about 13 yr. This possible activity cycle indicates that the two data sets analysed in Paper I (2004.9 and 2005.9) occurred at activity minimum (spanning from late-2004 to late-2007), whereas the data set analysed in this paper (2014.9/2015.1) took place close to activity maximum (spanning from late-2011 to late-2014). Such scenario is indeed corroborated by our large-scale magnetic field maps. We find that the averaged unsigned magnetic field strength increased by about 2.2 times from the two first epochs (at activity minimum) to the last epoch (at activity maximum). No such modulation is visible in the brightness maps, which display a spot coverage of 14%, 17%, and 18% in 2004.9, 2005.9, and 2014.9/2015.1, respectively. This result emphasizes that spot coverage may not always be an appropriate observable to study activity cycles in very active rapidly rotating stars.

The analysis of the $H\alpha$ emission in 2014.9/2015.1 shows a prominence located farther than the Lagrange point L1 towards the white dwarf component, and that remained stable during the entire observation window (44 rotation cycles). The prominence size and location we infer are consistent within error bars with the prominence properties derived in 2004.9 (Paper I). Using the prominence flux in $H\alpha$ of $1.1 \times 10^{-13} \text{ erg s}^{-1} \text{ cm}^{-2}$, we derive a prominence mass of $4 \times 10^{18} \text{ g}$ in 2014.9/2015.1 slightly smaller than that identified in 2004.9 of $6 \times 10^{18} \text{ g}$ (see Equation 3 in Steeghs et al. 1996). The prominence mass-range of $4\text{--}6 \times 10^{18} \text{ g}$ is broadly consistent with those derived for other K dwarf stars hosting prominences – e.g. K0 dwarf AB Dor ($2\text{--}10 \times 10^{17} \text{ g}$, e.g., Collier Cameron & Robinson 1989; Collier Cameron et al. 1990) and the K3 dwarf Speedy Mic ($0.5\text{--}2.3 \times 10^{17} \text{ g}$, Dunstone et al. 2006).

As illustrated in Figure 7, the potential field extrapolation of the radial magnetic field map that we derived for the K2 dwarf shows closed loops of magnetic field that extend out from the surface and reach the prominence location. This result is consistent with that of Paper I and offers further qualitative proof that a slingshot mechanism is likely responsible for confining the prominence further away from the center of mass of the system and from the Lagrange point L1 (located at $1.679 \pm 0.004 R_\star$ and $1.84 \pm 0.02 R_\star$ from the center of the K2 dwarf star, respectively). Slingshot mechanisms have been also suggested to operate in single fast-rotating stars hosting prominences at a few stellar radii above the stellar surface (see discussion in Jardine & Collier Cameron 2019), such as AB Dor (Collier Cameron & Robinson 1989; Waugh & Jardine 2019), HK Aqu (Byrne et al. 1996), LQ Lup (Donati et al. 2000), Speedy Mic (Dunstone et al. 2006; Waugh & Jardine 2019), V374 Peg (Vida et al. 2016), and V530 Per (Cang et al. 2020, 2021).

Altogether, the potential field extrapolations available for the K2 dwarf V471 Tau show that when a prominence is seen in the system (2004.9 and 2014.9/2015.1) close loops of magnetic lines reach the prominence location, whereas when no prominence is detected (2005.9) only open field lines are found at the expected prominence location (see details about previous reconstructions in Paper I). This finding indicates that the evolution of the large-scale magnetic field controls the rate at which stable prominences are generated in V471 Tau.

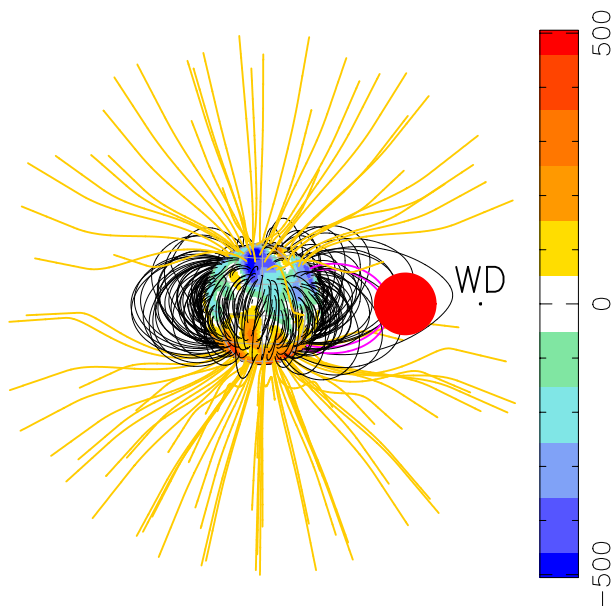


Figure 7. Potential field extrapolation of the large-scale radial magnetic field reconstruction of the K2 dwarf obtained with ZDI in 2014.9/2015.1. Field lines are seen at rotational phase 0.75 and are shown in yellow/black when the lines are open/closed. The prominence is illustrated as a red circle, and the field lines crossing the prominence are coloured in magenta. The local surface field strength (G) of the star is shown in colours and follows the colour scale on the right. A black circle indicates the white dwarf (WD) position; however, its magnetic field is not considered in the potential field extrapolation.

4.3 ETVs in V471 Tau

The observed minus computed (O-C) eclipse timings available in the literature for V471 Tau (cross symbols) are illustrated in Figure 8. The data evidence the periodic behaviour of the ETVs in V471 Tau with current observations yielding a modulation period of 30–40 yr (Guinan & Ribas 2001; İbanoğlu et al. 2005; Kundra & Hric 2011; Marchioni et al. 2018) and an O-C amplitude ranging from 130 to 200 s (Kundra & Hric 2011; Marchioni et al. 2018) depending on the ephemeris employed. To compare this trend with independent measures, we use the phase offsets ϕ_0 available in the literature for V471 Tau to infer the O-C amplitude. These two quantities are expected to scale as

$$\text{O-C} = \phi_0 \times P_{\text{orb}}. \quad (3)$$

We find an O-C amplitude of 158 ± 90 s in 2002.9 (green circle, Hussain et al. 2006), 180 ± 9 s in 2004.9 (red, Paper I), 158 ± 9 s in 2005.9 (blue, Paper I), and 113 ± 23 s in 2014.9/2015.1 (yellow, this paper).

The O-C values that we infer from Equation 3 agree with the trend found using long-term photometry. They offer an independent validation of the ETVs in V471 Tau as all the four phase offset measurements considered take into account the presence of spots at the surface of the K2 dwarf (see Section 3) that may otherwise affect the eclipse timing measurements from photometry (Kalimeris et al. 2002). Furthermore, the intermediate value of O-C that we infer in 2014.9/2015.1 suggests that although the orbital period of the system was decreasing from 2002.9 to 2015.1, it did not reach the minimum orbital period recorded for V471 Tau (which took place around 1980, i.e. when O-C crosses 0 going to negative values). As a result, the

observation reported in this paper did not probe the ETV cycle at the phase of largest surface differential rotation as predicted if an Applegate mechanism is indeed operating on V471 Tau. This result is corroborated by the eclipse timing measure using photometric data from the K2 mission acquired around 2015.2, which yields O-C = 169 s.

Similar to the findings of Paper I, we detect a relative differential rotation in 2014.9/2015.1 of $d\Omega/\Omega_{\text{eq}} = 0.5\%$ and 0.4% using Stokes I and Stokes V , respectively. These values are weaker than what is needed for the feasibility of an Applegate mechanism in V471 Tau. Considering the range of shears currently measured at the surface of the K2 dwarf (ranging from 0.4 to 1.1%), the Applegate mechanism would drive ETVs with a semi-amplitude of $\Delta P/P_{\text{orb}} \lesssim 10^{-7}$ (Völschow et al. 2018) whereas V471 Tau displays $\Delta P/P_{\text{orb}} \approx 8.5 \times 10^{-7}$. Nevertheless, our O-C estimation in 2014.9/2015.1 indicates that the system was not orbiting at the minimum orbital period expected for V471 Tau (i.e., when the largest surface shear is expected in the framework of the Applegate mechanism). It may be possible that higher values of $d\Omega/\Omega_{\text{eq}}$ occur at the surface of the K2 dwarf and thus that the Applegate mechanism may indeed be at work.

We suggest that spectropolarimetric observations in the upcoming years will help understand whether the ETVs in V471 Tau are magnetically-driven especially if they can probe the ETV cycle at the expected phase of largest differential rotation. Along with the tomographic maps already reconstructed for the K2 dwarf, it will be possible to further investigate whether the ETVs of V471 Tau are caused by the mechanism proposed by Applegate (1992) or by Lanza (2020). For this purpose, observations of V471 Tau were recently collected with ESPaDOnS in 2021B.

ACKNOWLEDGEMENTS

We thank the anonymous referee for helping improve and clarify this manuscript. This project received funding from the European Research Council (ERC) under the H2020 research & innovation programme (grant agreements #740651 New-Worlds and #865624 GPRV). This paper is based on observations obtained at the Canada-France-Hawaii Telescope (CFHT) which is operated by the National Research Council of Canada, the Institut National des Sciences de l’Univers of the Centre National de la Recherche Scientifique of France, and the University of Hawaii. The observations at the CFHT were performed with care and respect from the summit of Maunakea which is a significant cultural and historic site.

DATA AVAILABILITY

This paper includes data collected by the ESPaDOnS spectropolarimeter, which is publicly available from the Canadian Astronomy Data Center (program IDs: 15AP15 & 14BP15).

REFERENCES

- Alvarado-Gómez J. D., et al., 2015, *A&A*, **582**, A38
- Applegate J. H., 1992, *ApJ*, **385**, 621
- Applegate J. H., Patterson J., 1987, *ApJ*, **322**, L99
- Bours M. C. P., et al., 2016, *MNRAS*, **460**, 3873
- Brown S. F., Donati J. F., Rees D. E., Semel M., 1991, *A&A*, **250**, 463
- Byrne P. B., Eibe M. T., Rolleston W. R. J., 1996, *A&A*, **311**, 651
- Cang T. Q., et al., 2020, *A&A*, **643**, A39

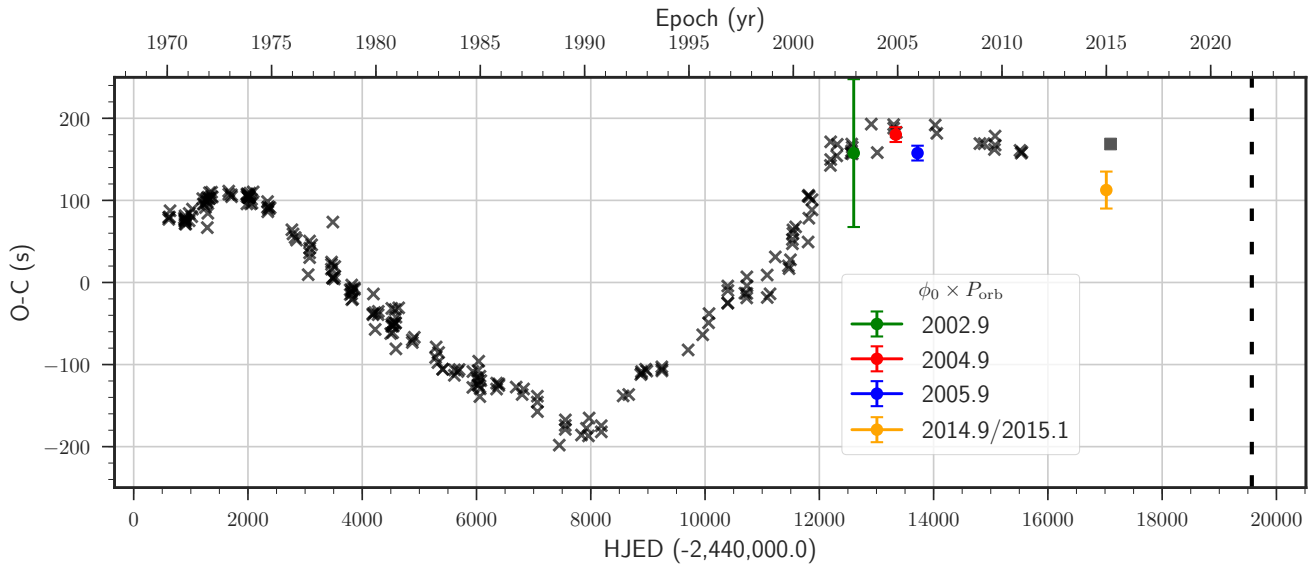


Figure 8. Observed minus computed eclipse timing variations of V471 Tau assuming the linear ephemeris given by Equation 1. Crosses represent O-C measurements from eclipse timings and circles the O-C values estimated from the phase offset ϕ_0 multiplied by the orbital period (shown with $1-\sigma$ errorbars). The black square gives the single eclipse timing measure using K2 data (Muirhead et al. 2021), corresponding to HJD 2457097.1816484 in Terrestrial Time (TT) scale (see Eastman et al. 2010). The vertical dashed line marks the recent observation campaign of V471 Tau with ESPaDOnS (2021B).

- Cang T. Q., Petit P., Donati J. F., Folsom C. P., 2021, *A&A*, **654**, A42
- Collier Cameron A., Robinson R. D., 1989, *MNRAS*, **238**, 657
- Collier Cameron A., Duncan D. K., Ehrenfreund P., Foing B. H., Kuntz K. D., Penston M. V., Robinson R. D., Soderblom D. R., 1990, *MNRAS*, **247**, 415
- Conroy K. E., Prša A., Stassun K. G., Orosz J. A., Fabrycky D. C., Welsh W. F., 2014, *AJ*, **147**, 45
- Donati J. F., 2003, in Trujillo-Bueno J., Sanchez Almeida J., eds, *Astronomical Society of the Pacific Conference Series Vol. 307, Solar Polarization*. p. 41
- Donati J. F., Brown S. F., 1997, *A&A*, **326**, 1135
- Donati J. F., Semel M., Praderie F., 1989, *A&A*, **225**, 467
- Donati J. F., Semel M., Carter B. D., Rees D. E., Collier Cameron A., 1997, *MNRAS*, **291**, 658
- Donati J.-F., Mengel M., Carter B. D., Marsden S., Collier Cameron A., Wichmann R., 2000, *MNRAS*, **316**, 699
- Donati J. F., Collier Cameron A., Petit P., 2003, *MNRAS*, **345**, 1187
- Donati J. F., Catala C., Landstreet J. D., Petit P., 2006a, in Casini R., Lites B. W., eds, *Astronomical Society of the Pacific Conference Series Vol. 358, Solar Polarization 4*. p. 362
- Donati J.-F., et al., 2006b, *MNRAS*, **370**, 629
- Dunstone N. J., Collier Cameron A., Barnes J. R., Jardine M., 2006, *MNRAS*, **373**, 1308
- Eastman J., Siverd R., Gaudi B. S., 2010, *PASP*, **122**, 935
- Guinan E. F., Ribas I., 2001, *ApJ*, **546**, L43
- Hahlin A., Kochukhov O., Alecian E., Morin J., BinaMIcS Collaboration 2021, *A&A*, **650**, A197
- Hajdu T., Borkovits T., Forgács-Dajka E., Sztakovics J., Marschalló G., Kutrovátz G., 2019, *MNRAS*, **485**, 2562
- Hardy A., et al., 2015, *ApJ*, **800**, L24
- Horner J., Marshall J. P., Wittenmyer R. A., Tinney C. G., 2011, *MNRAS*, **416**, L11
- Horner J., Hinse T. C., Wittenmyer R. A., Marshall J. P., Tinney C. G., 2012, *MNRAS*, **427**, 2812
- Horner J., Wittenmyer R., Hinse T., Marshall J., Mustill A., 2014, arXiv e-prints, p. arXiv:1401.6742
- Hussain G. A. J., Allende Prieto C., Saar S. H., Still M., 2006, *MNRAS*, **367**, 1699
- İbanoğlu C., Evren S., Taş G., Çakırlı Ö., 2005, *MNRAS*, **360**, 1077
- Irwin J. B., 1952, *ApJ*, **116**, 211
- Jardine M., Collier Cameron A., 2019, *MNRAS*, **482**, 2853
- Kővári Z., et al., 2021, *A&A*, **650**, A158
- Kalimeris A., Rovithis-Livanou H., Rovithis P., 2002, *A&A*, **387**, 969
- Kamiński K. Z., et al., 2007, *The Astronomical Journal*, **134**, 1206–1215
- Kundra E., Hric L., 2011, *Ap&SS*, **331**, 121
- Landi Degl'Innocenti E., Landolfi M., 2004, *Line Formation in a Magnetic Field*. Springer Netherlands, Dordrecht, pp 375–507, doi:10.1007/1-4020-2415-0_9, https://doi.org/10.1007/1-4020-2415-0_9
- Lanza A. F., 2005, *MNRAS*, **364**, 238
- Lanza A. F., 2006, *MNRAS*, **369**, 1773
- Lanza A. F., 2020, *MNRAS*, **491**, 1820
- Lanza A. F., Rodonò M., 1999, *A&A*, **349**, 887
- Lanza A. F., Rodono M., Rosner R., 1998, *MNRAS*, **296**, 893
- Lehmann L. T., Hussain G. A. J., Jardine M. M., Mackay D. H., Vidotto A. A., 2019, *MNRAS*, **483**, 5246
- Mai X., Mutel R. L., 2021, arXiv e-prints, p. arXiv:2110.14869
- Marcadon F., Helminiak K. G., Marques J. P., Pawłaszek R., Sybilski P., Kozłowski S. K., Ratajczak M., Konacki M., 2020, *MNRAS*, **499**, 3019
- Marchioni L., Guinan E. F., Engle S. G., Dowling Jones L., Michail J. M., Werner G., Ribas I., 2018, *Research Notes of the American Astronomical Society*, **2**, 179
- Marsh T. R., 2018, *Circumbinary Planets Around Evolved Stars*. Springer International Publishing, pp 2731–2747, doi:10.1007/978-3-319-55333-7_96
- Marsh T. R., et al., 2014, *MNRAS*, **437**, 475
- Muirhead P. S., Nordhaus J., Drout M. R., 2021, arXiv e-prints, p. arXiv:2111.06905
- Navarrete F. H., Schleicher D. R. G., Zamponi Fuentealba J., Völschow M., 2018, *A&A*, **615**, A81
- Navarrete F. H., Schleicher D. R. G., Käpylä P. J., Schober J., Völschow M., Mennickent R. E., 2020, *MNRAS*, **491**, 1043
- Nelson B., Young A., 1970, *PASP*, **82**, 699
- Pandey J. C., Singh K. P., 2008, *MNRAS*, **387**, 1627
- Papageorgiou A., Catelan M., Christopoulou P.-E., Drake A. J., Djorgovski

- S. G., 2021, *MNRAS*, **503**, 2979
- Parsons S. G., et al., 2010, *MNRAS*, **407**, 2362
- Ramseyer T. F., Hatzes A. P., Jablonski F., 1995, *AJ*, **110**, 1364
- Rappaport S., Deck K., Levine A., Borkovits T., Carter J., El Mellah I., Sanchis-Ojeda R., Kalomeni B., 2013, *ApJ*, **768**, 33
- Rice J. B., Wehlau W. H., Khokhlova V. L., 1989, *A&A*, **208**, 179
- Rottler L., Batalha C., Young A., Vogt S., 2002, *A&A*, **392**, 535
- Skillman D. R., Patterson J., 1988, *AJ*, **96**, 976
- Steehgs D., Horne K., Marsh T. R., Donati J. F., 1996, *MNRAS*, **281**, 626
- Unruh Y. C., Collier Cameron A., 1995, *MNRAS*, **273**, 1
- Vaccaro T. R., Wilson R. E., Van Hamme W., Terrell D., 2015, *ApJ*, **810**, 157
- Vanderbosch Z. P., Clemens J. C., Dunlap B. H., Winget D. E., 2017, in Tremblay P. E., Gaensicke B., Marsh T., eds, *Astronomical Society of the Pacific Conference Series Vol. 509, 20th European White Dwarf Workshop*, pp 571–574
- Vida K., et al., 2016, *A&A*, **590**, A11
- Vincent A., Piskunov N. E., Tuominen I., 1993, *A&A*, **278**, 523
- Vogt S. S., Penrod G. D., Hatzes A. P., 1987, *ApJ*, **321**, 496
- Völschow M., Schleicher D. R. G., Perdelwitz V., Banerjee R., 2016, *A&A*, **587**, A34
- Völschow M., Schleicher D. R. G., Banerjee R., Schmitt J. H. M. M., 2018, *A&A*, **620**, A42
- Waugh R. F. P., Jardine M. M., 2019, *MNRAS*, **483**, 1513
- Wittenmyer R. A., Horner J., Marshall J. P., Butters O. W., Tinney C. G., 2012, *MNRAS*, **419**, 3258
- Young A., Rottler L., Skumanich A., 1991, *ApJ*, **378**, L25
- Zaire B., Donati J. F., Klein B., 2021, *MNRAS*, **504**, 1969
- Zorotovic M., Schreiber M. R., 2013, *A&A*, **549**, A95
- Şenavcı H. V., Bahar E., Montes D., Zola S., Hussain G. A. J., Frasca A., Işık E., Yörükoğlu O., 2018, *MNRAS*, **479**, 875

APPENDIX A: JOURNAL OF OBSERVATIONS

The logbook of the spectropolarimetric observations of V471 Tau used in this study is shown in Table A1.

APPENDIX B: STOKES SIGNATURES

Stokes I and Stokes V profiles are given in Figures B1 and B2, respectively. Observed Stokes LSD profiles are shown in red, and modelled Stokes profiles are given in black. Modelled Stokes signatures are associated with the surface maps obtained through independent ZDI reconstructions using either the spectropolarimetric data set of December 2014 (top panels in Figure 4) or January 2015 (bottom panels in Figure 4).

This paper has been typeset from a $\text{\TeX}/\text{\LaTeX}$ file prepared by the author.

Table A1. Summary of ESPaDOnS/CFHT observations for V471 Tau from December 2014 to January 2015. Columns 1 to 4 respectively record (i) the date of observation, (ii) the UT time at mid sub-exposure, (iii) the time in Heliocentric Julian Date (HJD), and (iv) the rotation cycle of each observation. Column 5 illustrates peak SNR values for the Stokes V spectrum (per 1.8 km/s spectral pixel). Column 6 shows the RMS noise level of the Stokes V LSD profile.

Date	UT (h:m:s)	HJD (2, 453, 337+)	E (21, 470+)	SNR	σ_{LSD} (10^{-4})
20 Dec 2014	06:17:40	3674.76735	0.118441	202	1.5
20 Dec 2014	06:35:24	3674.77967	0.142079	207	1.5
20 Dec 2014	06:53:09	3674.79199	0.165718	200	1.5
20 Dec 2014	12:05:19	3675.00877	0.581656	137	2.5
20 Dec 2014	12:23:04	3675.02109	0.605294	134	2.5
20 Dec 2014	12:40:48	3675.03340	0.628914	122	2.9
21 Dec 2014	05:41:49	3675.74239	1.989260	194	1.6
21 Dec 2014	05:59:33	3675.75471	2.012899	195	1.6
21 Dec 2014	06:17:18	3675.76704	2.036556	193	1.6
21 Dec 2014	11:29:48	3675.98404	2.452917	182	1.8
21 Dec 2014	11:47:33	3675.99636	2.476555	179	1.8
21 Dec 2014	12:05:17	3676.00868	2.500194	165	2.0
22 Dec 2014	06:40:09	3676.78284	3.985582	187	1.7
22 Dec 2014	06:57:53	3676.79515	4.009202	196	1.6
22 Dec 2014	07:15:38	3676.80748	4.032859	198	1.6
22 Dec 2014	12:26:57	3677.02366	4.447646	176	1.9
22 Dec 2014	12:44:42	3677.03598	4.471285	178	1.9
22 Dec 2014	13:02:26	3677.04830	4.494923	157	2.1
28 Dec 2014	08:56:52	3682.87737	15.679221	205	1.5
28 Dec 2014	09:14:36	3682.88968	15.702840	209	1.5
28 Dec 2014	09:32:20	3682.90200	15.726479	184	1.7
29 Dec 2014	06:02:07	3683.75595	17.364961	196	1.6
29 Dec 2014	06:19:52	3683.76827	17.388600	198	1.6
29 Dec 2014	06:37:36	3683.78059	17.412238	189	1.6
29 Dec 2014	11:46:02	3683.99477	17.823188	194	1.6
29 Dec 2014	12:03:47	3684.00709	17.846826	191	1.7
29 Dec 2014	12:21:32	3684.01941	17.870465	182	1.8
30 Dec 2014	04:34:15	3684.69486	19.166458	193	1.6
30 Dec 2014	04:52:01	3684.70719	19.190115	196	1.6
30 Dec 2014	05:09:45	3684.71951	19.213754	203	1.6
30 Dec 2014	10:24:43	3684.93823	19.633414	210	1.5
30 Dec 2014	10:42:28	3684.95055	19.657053	210	1.5
30 Dec 2014	11:00:12	3684.96287	19.680691	212	1.5
07 Jan 2015	05:43:50	3692.74255	34.607644	133	2.5
07 Jan 2015	06:01:37	3692.75490	34.631341	138	2.4
07 Jan 2015	06:19:24	3692.76725	34.655037	168	1.9
07 Jan 2015	11:29:05	3692.98230	35.067655	162	2.0
07 Jan 2015	11:46:50	3692.99461	35.091275	152	2.2
07 Jan 2015	12:04:35	3693.00694	35.114932	144	2.3
08 Jan 2015	04:44:36	3693.70134	36.447285	202	1.6
08 Jan 2015	05:02:30	3693.71377	36.471134	202	1.6
08 Jan 2015	05:20:14	3693.72609	36.494773	202	1.5
08 Jan 2015	10:30:48	3693.94174	36.908543	191	1.7
08 Jan 2015	10:48:33	3693.95406	36.932181	188	1.7
08 Jan 2015	11:06:18	3693.96639	36.955839	191	1.7
09 Jan 2015	04:39:52	3694.69797	38.359529	189	1.7
09 Jan 2015	04:57:37	3694.71030	38.383187	189	1.7
09 Jan 2015	05:15:22	3694.72262	38.406825	193	1.6
09 Jan 2015	10:24:48	3694.93749	38.819099	191	1.7
09 Jan 2015	10:42:34	3694.94982	38.842756	190	1.7
09 Jan 2015	11:00:19	3694.96215	38.866414	178	1.8
10 Jan 2015	04:40:42	3695.69846	40.279180	182	1.7
10 Jan 2015	04:58:27	3695.71079	40.302838	177	1.8
10 Jan 2015	05:16:11	3695.72311	40.326476	183	1.8
10 Jan 2015	10:26:58	3695.93890	40.740515	190	1.7
10 Jan 2015	10:44:43	3695.95123	40.764172	190	1.7
10 Jan 2015	11:02:29	3695.96356	40.787830	180	1.8
12 Jan 2015	10:25:28	3697.93769	44.575614	198	1.6
12 Jan 2015	10:43:13	3697.95002	44.599271	195	1.7

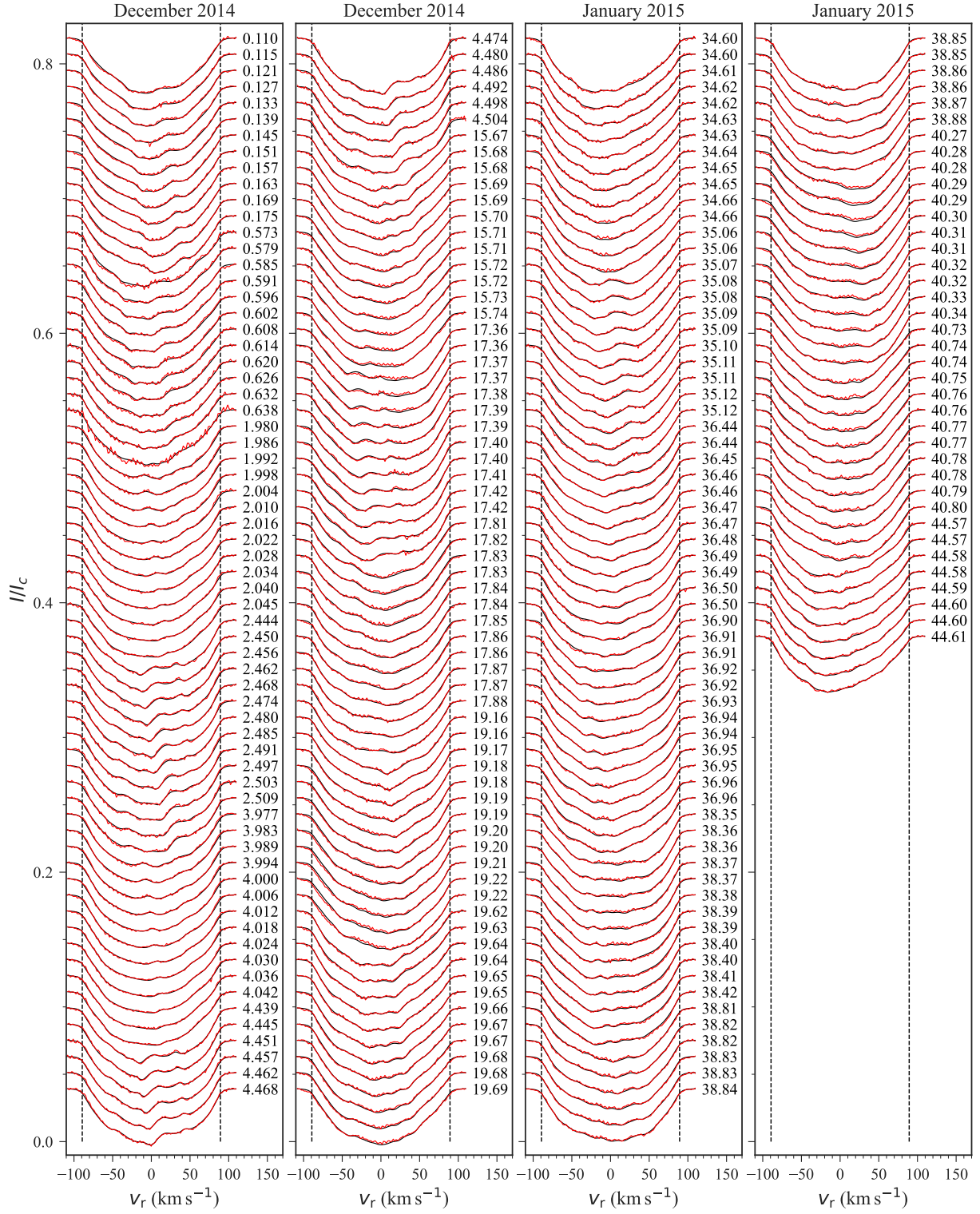


Figure B1. Stokes I profiles in 2014.9 (columns 1 and 2) and 2015.1 (columns 3 and 4) data sets. Observed Stokes I LSD profiles are shown in red, whereas modelled observations are shown in black (see Section 3.1.1 for further details). All profiles are equally shifted for illustration purposes. The rotation cycle of each observation is shown in the right.

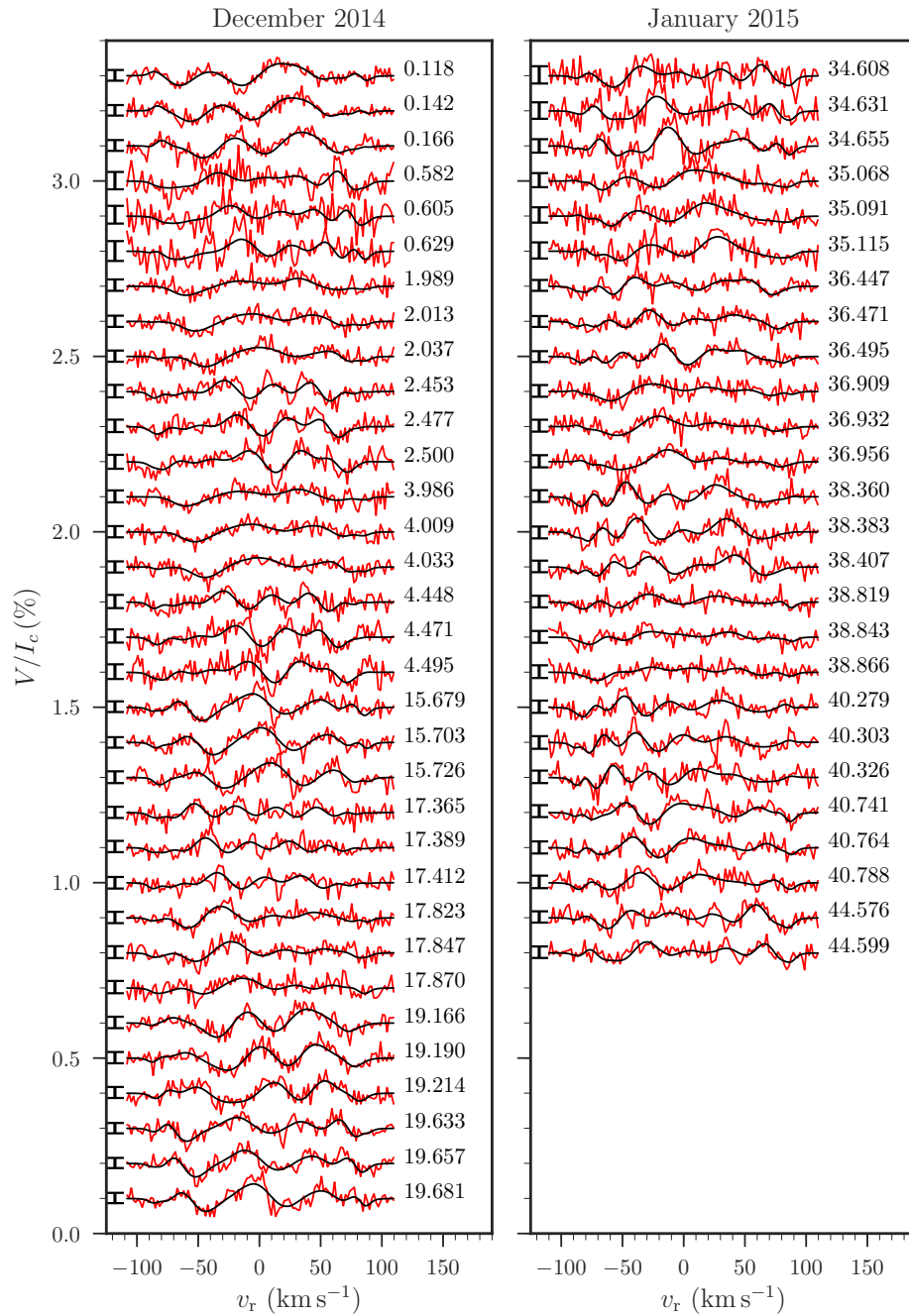


Figure B2. Stokes V profiles in 2014.9 (left) and 2015.1 (right) data sets. Observed Stokes V LSD profiles are shown in red, whereas modelled observations are shown in black (see Section 3.1.1 for further details). All profiles are equally shifted for illustration purposes. The rotation cycle of each observation is shown in the right and 1σ error bars in the left.